PCC and EKF-Based Pipe-Climbing Simulation of Kresling Origami Continuum Robots

Shuhan Guo
{gshuhan}@umich.edu

***Abstract*—This paper presents a simulation framework for pipe-climbing continuum robots based on origami-inspired Kresling chambers. A Piecewise Constant Curvature (PCC) model is employed to compute closed-form forward kinematics of each section under arbitrary tendon inputs. An Extended Kalman Filter (EKF) fuses noisy IMU orientation measurements with the PCC predictions to produce drift-corrected pose estimates, while a simple collision-based mode-switch rule enforces realistic gait by halting lateral motion upon wall contact and swapping the fixed disk. Simulation studies do the EKF and demonstrate near-linear vertical climb within a 0.18m-radius pipe without wall penetration. The results validate the accuracy of PCC kinematics, the benefit of EKF fusion, and the effectiveness of the collision-based switching strategy for confined continuum robot locomotion.**

***Index Terms*—Continuum robots, Kresling origami, piecewise constant curvature (PCC), extended Kalman filter (EKF), pipe climbing, state estimation, GTSAM, collision-based mode switching**

I. Introduction

Continuum robots have attracted significant attention in recent years for their ability to navigate and manipulate within highly constrained environments such as pipelines, blood vessels, and industrial ducts. Unlike traditional rigid-link manipulators, continuum robots achieve compliance and dexterity through continuously deformable backbones or segmental architectures, enabling smooth adaptation to complex geometries [1], [2]. Among these, origami-inspired Kresling structures offer a particularly attractive combination of lightweight construction, large bending capability, and tunable stiffness by controlling tendon lengths [3].

Climbing inside vertical or inclined pipes is a canonical application for continuum robots, with relevance to inspection, maintenance, and medical devices. Prior work has demonstrated various actuation schemes—including pneumatic chambers, tendon-driven backbones, and magnetically actuated modules—to achieve peristaltic or inchworm-style locomotion [2]. However, accurately predicting and controlling the shape of such robots in real time remains challenging due to sensor noise, modeling uncertainties, and intermittent wall contact.

This paper presents a simulation framework that integrates three key components:

1) **Piecewise Constant Curvature (PCC) kinematics**, which provides closed-form forward kinematic predictions of the Kresling origami shape under arbitrary tendon inputs.
2) **Extended Kalman Filter (EKF)–based state estimation**, which fuses noisy IMU orientation measurements with PCC model predictions to produce drift-corrected estimates of the robot's pose.
3) **Collision-based mode switching**, a simple yet effective rule that halts lateral deformation upon pipe contact and swaps the "stuck" disk, thereby enforcing a realistic pipe-climbing gait.

This project further compares the EKF approach against a factor-graph optimization using GTSAM to highlight trade-offs in accuracy and computational cost. Simulation results demonstrate that the combined PCC+EKF framework yields smooth, accurate trajectories both in free space and within a 0.18m-radius pipe, preserving near-linear vertical progression while avoiding wall penetration.

The code is publicly available at: *https://github.com/Shuhan1221/ROB-590.git*.

II. Literature Review

Recent advances in continuum robotics have addressed key challenges related to accurate state estimation, actuation, and proprioceptive sensing. Lilge et al. [1] introduced a robust state estimation method for continuum multirobot systems utilizing Gaussian process regression on SE(3), efficiently managing complex coupled topologies, with high accuracy and computational performance suitable for real-time scenarios. Complementing this, Stella et al. [2] proposed an IMU-based drift-filtering algorithm leveraging the piecewise constant curvature (PCC) assumption, substantially improving shape reconstruction accuracy and enabling reliable closed-loop control despite inherent IMU drift issues. Furthermore, Fan et al. [3] developed a novel vacuum-driven parallel continuum robot (PCR) employing self-sensing origami linkages fabricated via soft-rigid hybrid 3D printing. This innovative design demonstrated multimodal motion, significant load-carrying capabilities, and high positioning accuracy without reliance on external sensing. Collectively, these studies underscore substantial progress in continuum robotics by integrating advanced modeling, sensing, and actuation techniques, enhancing overall robotic system performance and reliability.

III. Methodology

A. PCC Forward-Kinematic Simulation of a Kresling Origami Chamber

We perform forward kinematics by starting from the three tendon lengths $\{l_1, l_2, l_3\}$ at the base and propagating through

N PCC sections to obtain the final state

$$\{(x_k, y_k, z_k, \phi_k, \theta_k, \psi_k)\}_{k=1}^{N}.$$

The positions (x_k, y_k, z_k) trace the 3D path of the end-disk, while $(\phi_k, \theta_k, \psi_k)$ give its roll–pitch–yaw orientation.

1. Section-Level Bending & Twisting: From the current section tendon lengths $(l_{1,k}, l_{2,k}, l_{3,k})$, compute

$$\varphi_k = \frac{2}{3\,r}\sqrt{\sum_{i=1}^{3} l_{i,k}^2 \;-\; \sum_{1\le i<j\le 3} l_{i,k}\, l_{j,k}}, \tag{1}$$

$$\beta_k = \operatorname{atan2}\big(3\,(l_{2,k} - l_{3,k}),\ \sqrt{3}\,(2\,l_{1,k} - l_{2,k} - l_{3,k})\big). \tag{2}$$

Here φ_k is the bending-plane angle and β_k the total bend for section k.

2. Constant-Curvature Pose: Define the rotation matrix

$$R(\beta, \varphi) \;=\; \big[\; c_1 \;\big|\; c_2 \;\big|\; c_3 \big] \tag{3}$$

where

$$c_1 := \begin{pmatrix} \cos\beta\,\cos^2\varphi + \sin^2\varphi \\ (\cos\beta - 1)\cos\varphi\sin\varphi \\ \cos\varphi\,\sin\beta \end{pmatrix},$$

$$c_2 := \begin{pmatrix} (\cos\beta - 1)\cos\varphi\sin\varphi \\ \cos\beta\,\sin^2\varphi + \cos^2\varphi \\ \sin\varphi\,\sin\beta \end{pmatrix},$$

$$c_3 := \begin{pmatrix} -\cos\varphi\,\sin\beta \\ -\sin\varphi\,\sin\beta \\ \cos\beta \end{pmatrix},$$

and the section offset

$$\mathbf{d}_k = \frac{1}{\rho_k}\begin{pmatrix} (1-\cos\beta_k)\sin\varphi_k \\ (1-\cos\beta_k)\cos\varphi_k \\ \sin\beta_k \end{pmatrix},$$

where $\rho_k = \beta_k/\bar{\ell}_k$ and $\bar{\ell}_k = (l_{1,k} + l_{2,k} + l_{3,k})/3$.

3. Tip Pose and Orientation: Attaching a rigid link of length L_{rigid} to section k yields

$$\mathbf{p}_k = \mathbf{p}_{k-1} + R_k \begin{pmatrix} 0 \\ 0 \\ L_{\text{rigid}} \end{pmatrix} + \mathbf{d}_k,$$

$$(\phi_k, \theta_k, \psi_k) = \text{RotMat2Euler}\big(R_k\big),$$

with $\mathbf{p}_0$ the known base position. Iterate for $k = 1, \ldots, N$ to build the full kinematic chain.

B. Trajectory Prediction via Extended Kalman Filter

1. Definitions: State and covariance:

$$\mu_k = [\, x_k, y_k, z_k, \phi_k, \theta_k, \psi_k \,]^\top, \quad \Sigma_k = \text{Cov}(\mu_k).$$

Control and measurement:

$$u_k = [\, l_{1,k}, l_{2,k}, l_{3,k} \,]^\top, \quad z_k = [\, \phi_k^{\text{imu}}, \theta_k^{\text{imu}}, \psi_k^{\text{imu}} \,]^\top.$$

2. Prediction Step:

a) State Prediction: Under PCC kinematics,

$$\mu_k^- = f(u_k, \mu_{k-1}) = \mu_{k-1} + \begin{bmatrix} \Delta x(u_k) \\ \Delta y(u_k) \\ \Delta z(u_k) \\ \varphi_k \\ \beta_k \\ 0 \end{bmatrix}, \tag{4}$$

and $\Delta\{x, y, z\}$ derive from $\mathbf{d}_k + R_k[0, 0, L_{\text{rigid}}]^\top$.

b) Covariance Prediction: Compute Jacobians

$$F_k = \frac{\partial f}{\partial \mu}\Big|_{\mu_{k-1}, u_k}, \quad W_k = \frac{\partial f}{\partial w}\Big|_{\mu_{k-1}, u_k},$$

then

$$\Sigma_k^- = F_k\,\Sigma_{k-1}\,F_k^\top + W_k\,Q_k\,W_k^\top, \tag{5}$$

with process-noise covariance Q_k.

3. Correction Step:

c) Innovation:

$$\nu_k = z_k - h(\mu_k^-), \quad h(\mu) = [\, \phi, \theta, \psi \,]^\top.$$

d) Innovation Covariance:

$$H_k = [\, 0_{3\times 3} \;\; I_3 \,],$$

$$S_k = H_k\,\Sigma_k^-\,H_k^\top + R_k. \tag{6}$$

e) Update:

$$K_k = \Sigma_k^-\,H_k^\top\,S_k^{-1}, \tag{7}$$

$$\mu_k = \mu_k^- + K_k\,\nu_k, \tag{8}$$

$$\Sigma_k = (I - K_k H_k)\,\Sigma_k^- + K_k\,R_k\,K_k^\top. \tag{9}$$

4. Recursion: Repeat for $k = 1, 2, \ldots$, tuning Q_k, R_k per sensor characteristics.

Iterate these updates over to obtain the filtered trajectory $\{(x_k, y_k, z_k, \phi_k, \theta_k, \psi_k)\}$. The sequence of (x_k, y_k, z_k) is the 3D path, and $(\phi_k, \theta_k, \psi_k)$ gives its orientation (roll/pitch/yaw).

C. Factor-Graph Optimization Using GTSAM

We estimate the sequence of section poses $\{\mathbf{X}_i\}_{i=0}^{N}$ with $\mathbf{X}_i = [\, \phi_i, \theta_i, \psi_i, x_i, y_i, z_i \,]^\top$ by constructing and solving a nonlinear factor graph.

1. Keys and Noise Models:

- **Keys:** Use GTSAM's `Symbol` or integer keys:

$$\texttt{Key}(i) = \texttt{Symbol}('X',\, i), \quad i = 0, \ldots, N.$$

- **Noise models:**

$$\Sigma_p = \sigma_p^2\, I_6, \quad \Sigma_m = \text{diag}(\sigma_\phi^2, \sigma_\theta^2, \sigma_\psi^2, \sigma_x^2, \sigma_y^2, \sigma_z^2), \quad \Sigma_c = \sigma_c^2\, I_6.$$

Choose $\sigma_p, \sigma_m, \sigma_c$ based on encoder/IMU precision.

2. Factors:

- **Prior on base pose:**

$$f_p^{(0)} = \|\mathbf{X}_0 - \mathbf{X}_0^{\text{init}}\|^2_{\Sigma_p}.$$

- **PCC-kinematics:** For each $i = 1 \dots N$,

$$e_{p,i} = \mathbf{X}_i - f(\mathbf{X}_{i-1}, u_i), \quad \|e_{p,i}\|^2_{\Sigma_p}.$$

- **Measurement:**

$$e_{m,i} = h(\mathbf{X}_i) - Z_i, \quad \|e_{m,i}\|^2_{\Sigma_m}.$$

- **Leg-end coupling:**

$$e_{c,i} = g(\mathbf{X}_{i,\text{leg}}, \mathbf{X}_{ee}), \quad \|e_{c,i}\|^2_{\Sigma_c}.$$

3. Optimization: Solve

$$\mathbf{X}^* = \arg\min_{\{\mathbf{X}_i\}} \sum_{i=0}^{N} \|e_{p,i}\|^2_{\Sigma_p} + \sum_{i=1}^{N} \|e_{m,i}\|^2_{\Sigma_m} + \sum_{i=1}^{N} \|e_{c,i}\|^2_{\Sigma_c}$$

using Levenberg–Marquardt with convergence tolerance ε and maximum iterations $K_{\max}$.

4. Covariance Recovery: After optimization, compute marginal covariances $\text{Cov}(\mathbf{X}_i)$ via the factor-graph's marginalization procedure.

5. Robustification and Online Estimation:

- Use robust kernels (e.g. Huber) on measurement and coupling factors to mitigate outliers.
- Tune $\sigma_p, \sigma_m, \sigma_c$ via cross-validation on experimental data.
- For real-time updates, employ an incremental solver (e.g. iSAM2) to update the graph as new measurements arrive.

D. Pipe-Climbing Simulation with EKF and Base Switching

We simulate a soft continuum robot climbing inside a vertical pipe by alternately "sticking" its disks to the wall. An EKF provides basic state estimation, but the core lies in managing the base switch.

1. Brief EKF Overview:

$$\mathbf{x}_k = [x_k, y_k, z_k, \phi_k, \theta_k, \psi_k]^\top, \quad P_{k|k} = \text{covariance}.$$

Predict/update steps follow standard EKF with tip-position measurements z_k and model Jacobians F_k, H.

2. Base-Switching Logic: Let $s_k \in \{0, 1\}$ indicate which disk is stuck:

$$s_k = \begin{cases} 0, & \text{bottom disk stuck,} \\ 1, & \text{top disk stuck.} \end{cases}$$

1) **After EKF update**, flip the flag: $s_{k+1} = 1 - s_k$.
2) **Compute inverse transform** of the last motion increment:

$$T_k^{-1} = \begin{bmatrix} R_k^\top & -R_k^\top \Delta p_k \\ 0_{1\times 3} & 1 \end{bmatrix}, \; \Delta p_k = \mathbf{d}_k + R_k [0, 0, L_{\text{link}}]^\top$$

3) **Rebase state:**

$$\hat{\mathbf{x}}_{k|k}^{\text{new}} = T_k^{-1} \, \hat{\mathbf{x}}_{k|k},$$

expressing the free-disk pose relative to the new stuck disk.

4) **Reset EKF covariance:** Rotate $P_{k|k}$ into the new frame:

$$P_{k|k}^{\text{new}} = \begin{bmatrix} R_k^\top & 0 \\ 0 & R_k^\top \end{bmatrix} P_{k|k} \begin{bmatrix} R_k & 0 \\ 0 & R_k \end{bmatrix}.$$

This focused base-switching ensures the EKF always operates in the current contact frame, yielding robust alternating-contact climbing estimation.

IV. Results

A. Trajectory and Direction Results

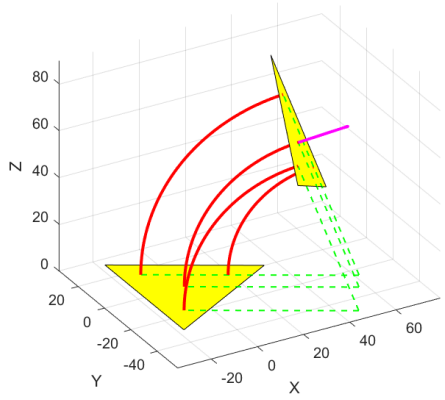

Fig. 1. PCC kinematic simulation of a Kresling origami chamber under the control input $u_1 = [60, 80, 100]^\top$. Yellow pyramidal meshes depict the base and end-effector disks; red curves trace the continuum bending of each kresling origami section; green dashed lines indicate the instantaneous curvature radii used in the PCC approximation; pink straight line refer to the orientation of effector

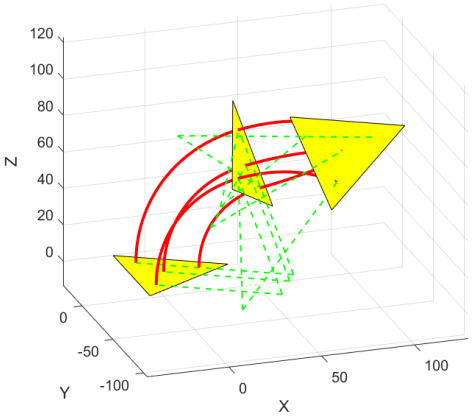

Fig. 2. Multi-layer PCC kinematic simulation of a Kresling origami chamber under the control input $u_1 = [60, 80, 100]^\top$ and $u_2 = [70, 50, 70]^\top$. Yellow pyramidal meshes depict the base and end-effector disks; red curves trace the continuum bending of each kresling origami section; green dashed lines indicate the instantaneous curvature radii used in the PCC approximation.

B. Analysis

Figures 1 and 2 demonstrate that the PCC model accurately captures the continuum bending of each Kresling origami

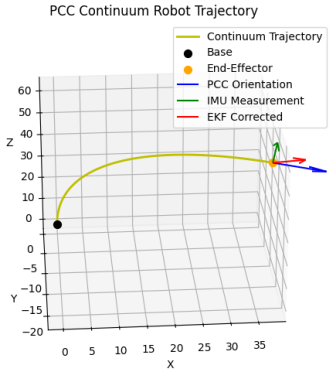

Fig. 3. Predicted trajectory of the center of the three-layer Kresling origami chamber (olive curve) under PCC kinematics. The control input is $u_1 = [60, 80, 100]^\top$The black marker denotes the fixed base, and the orange marker the end-effector. At the end-effector, three arrows illustrate orientation estimates: the blue arrow is the PCC-model orientation, the green arrow is the raw IMU measurement, and the red arrow is the EKF-corrected orientation.

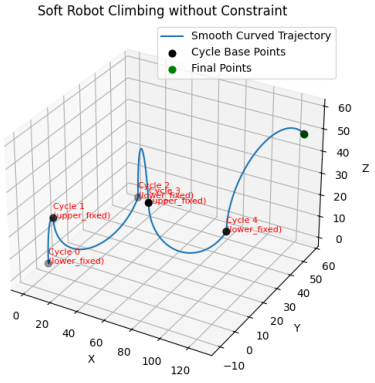

Fig. 4. Soft robot climbing without pipe constraint under the control-input sequence. $\{u_k\} = \{[20, 40, 60]^\top, [80, 10, 90]^\top, [45, 75, 120]^\top, [100, 20, 50]^\top, [60, 110, 30]^\top\}$ Blue shows the smooth curved trajectory, black circles mark the cycle base points, and the green dot indicates the final position.

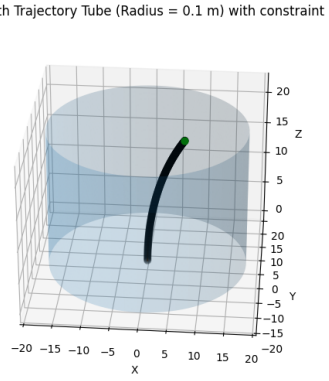

Fig. 5. Robot trajectory rendered as discrete points inside a semi-transparent pipe (inner radius = 0.18m, shown in light blue). Black points trace the EKF-constrained path, and the green marker denotes the final contact point.

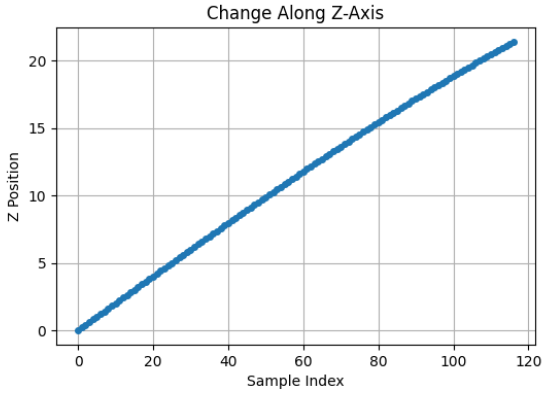

Fig. 6. Vertical progression of the EKF-constrained trajectory: Z-position versus sample index for the entire motion sequence.

section under both single-layer and multi-layer control inputs. In Fig. 1, the red arcs follow smooth constant-curvature paths between the base and end-effector disks, while the green dashed radii confirm that the locally fitted curvature β/ℓ matches the true deformation. Adding a second layer in Fig. 2 produces a more complex spatial coupling: the two arches overlap yet remain distinct, illustrating how upstream actuation (u_2) modifies the downstream chamber shape.

In Fig. 3 we overlay three independent orientation estimates at the end-effector: the PCC-model (blue), raw IMU (green), and EKF-corrected (red). The EKF successfully fuses the model prediction with noisy IMU readings, shifting the green arrow toward the PCC baseline. This correction reduces drift while preserving responsiveness to true bending.

Figures 4–7 compare the soft-robot climbing motion without (Fig. 4) and with (Figs. 5–7) a 0.18-radius pipe constraint. Unconstrained (Fig. 4), the robot traces a serpentine 3D arc, alternating "lower-fixed" and "upper-fixed" modes at each cycle base (black dots) and reaching a final height of approximately 50. When constrained (Fig. 5), however, collisions truncate lateral motion: each cycle stops as soon as the robot's 0.10-radius tube touches the wall, and mode switches occur earlier. The 2D plot of Z-position vs. sample index (Fig. 6) remains monotonic and nearly linear, indicating that vertical progress is only mildly affected by the contact events. Finally, the solid-tube rendering in Fig. 7 shows the full spatial envelope of the constrained motion, confirming that the robot remains entirely within the pipe bounds.

A second control-input sequence (Figs. 8–11) produces a more oscillatory climb: the robot first ascends to about 35, then descends slightly before a final rise to 40 (Fig. 10). The two-tone coloring in Fig. 11 (cyan for "lower-fixed," magenta for "upper-fixed") highlights how alternating anchor points and variable curvature can produce non-monotonic Z-profiles, even under continuous upward actuation.

Overall, these results validate that:

1) The PCC approximation yields smooth, analytically tractable kinematic predictions for both single- and

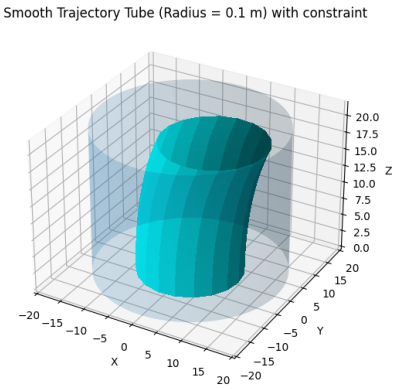

Fig. 7. Solid tube of radius 0.10m illustrating the smooth, pipe-constrained robot trajectory. The tube is rendered within the semi-transparent pipe (inner radius = 0.18m), showing the geometric envelope of motion under the same control inputs.

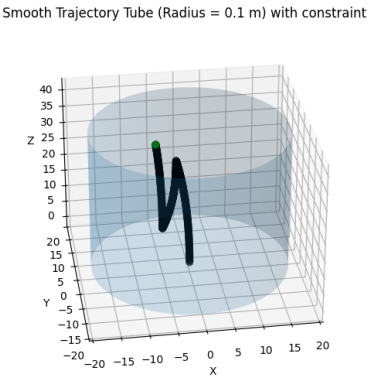

Fig. 9. Robot trajectory rendered as discrete points inside a semi-transparent pipe (inner radius = 0.18m, shown in light blue). Black points trace the EKF-constrained path, and the green marker denotes the final contact point.

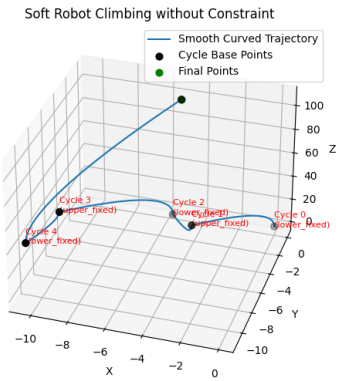

Fig. 8. Soft robot climbing without pipe constraint under the control-input sequence. $\{u_k\} = \{[40, 30, 40]^\top, [20, 20, 30]^\top, [50, 40, 50]^\top, [10, 20, 10]^\top, [60, 60, 60]^\top\}$ Blue shows the smooth curved trajectory, black circles mark the cycle base points, and the green dot indicates the final position.

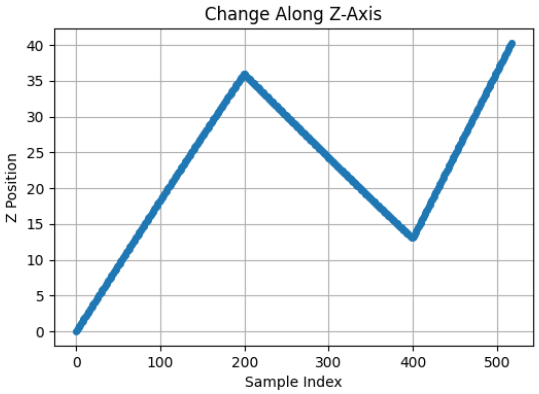

Fig. 10. Vertical progression of the EKF-constrained trajectory: Z-position versus sample index for the entire motion sequence.

multi-layer origami chambers.

2) EKF fusion enhances orientation accuracy by correcting raw IMU drift.
3) A simple collision-based mode-switch rule enables realistic simulation of pipe-climbing behavior, preserving vertical climb performance while automatically preventing wall penetration.

V. Discussion

The results presented above highlight several key insights and open avenues for further investigation:

a) Accuracy of the PCC approximation: Across both single-layer (Fig. 1) and multi-layer (Fig. 2) configurations, the Piecewise Constant Curvature (PCC) model reproduces the smooth, arch-shaped deformation of the Kresling origami sections with high fidelity. The constant-curvature arcs (red) align closely with the base and end-effector meshes, and the instantaneous radii (green dashed lines) confirm that the locally fitted curvature parameters β/ℓ capture the true geometric bending. This fidelity holds even when coupling two chambers in series, suggesting that the PCC assumption remains valid for moderate bending angles and multiple origami layers.

b) Benefits of EKF fusion: Figure 3 shows that raw IMU orientation measurements (green) exhibit noticeable jitter and drift relative to the ideal PCC model (blue). By incorporating the EKF-corrected estimate (red), we achieve a smoothed orientation that retains responsiveness to true bending while suppressing high-frequency noise. This fusion is crucial for tasks—such as closed-loop control or contact detection—where reliable orientation feedback is required.

c) Effect of pipe constraint on climbing performance: When unconstrained (Fig. 4), the robot follows a large lateral sweep before ascending, alternating "lower-fixed" and "upper-fixed" anchor modes at each cycle. Introducing a rigid pipe wall (radius = 0.18m) truncates these lateral motions (Fig. 5), forcing earlier mode transitions and reducing the overall horizontal excursion. Importantly, the vertical progression (Fig. 6) remains nearly linear and comparable in rate to

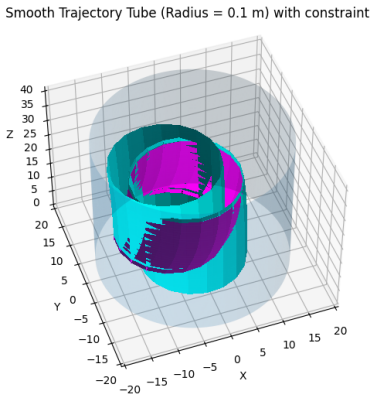

Fig. 11. Solid tube of radius 0.10m illustrating the smooth, pipe-constrained robot trajectory. The tube is rendered within the semi-transparent pipe (inner radius = 0.18m), showing the geometric envelope of motion under the same control inputs. The cyan color refers to the process of the lower fixed while the magenta color refers to the process of the upper fixed.

the unconstrained case, indicating that pipe contact does not substantially degrade climbing efficiency.

d) Mode-switch strategy and envelope generation: The simple collision-based rule—halt motion when $\|[x, y]\| + r_{\text{robot}} \geq r_{\text{pipe}}$, then swap "fixed" ends—proves effective at preventing wall penetration while preserving upward travel. The solid-tube renderings (Figs. 7 and 11) illustrate the full spatial envelope of motion under different control sequences. Notably, more aggressive or oscillatory inputs can produce non-monotonic Z-profiles (Fig. 10), suggesting that input scheduling can be used to tune both vertical speed and lateral clearance.

By combining the analytical tractability of PCC kinematics with robust EKF estimation and a simple yet effective collision rule, this framework offers a promising basis for design and control of continuum robots in constrained environments such as pipelines, boreholes, and confined biological conduits.

VI. Conclusion

This work has demonstrated the effectiveness of combining Piecewise Constant Curvature (PCC) kinematics, Extended Kalman Filter (EKF) state estimation, and a simple collision–based mode-switch rule to simulate and analyze the behavior of a continuum Kresling origami robot in both free and pipe-constrained environments. In particular:

- **PCC Kinematics Validated:** The PCC model reliably reproduces the smooth constant-curvature deformation of single- and multi-layer origami chambers (Figs. 1, 2), enabling closed-form computation of robot shape and end-effector pose.
- **EKF Improves Orientation Accuracy:** Fusing model-predicted orientation with noisy IMU measurements via an EKF yields a drift-corrected estimate (Fig. 3), critical for precise control and contact detection.
- **Realistic Pipe-Climbing:** Introducing a collision check that compares robot tube radius against pipe radius effectively halts lateral motion upon contact and triggers mode transitions, preventing wall penetration while preserving upward progression (Figs. 5–7).
- **Preserved Climb Performance:** Even under pipe constraints, vertical ascent remains nearly linear (Figs. 6, 10), demonstrating that lateral truncation does not unduly compromise climbing efficiency.
- **Design & Control Implications:** The simple framework presented here can guide the design of continuum robots for confined spaces, inform control-input scheduling to manage lateral clearance versus vertical speed, and serve as a foundation for experimental validation and extension to include frictional or compliant contact models.

Overall, the integration of analytical PCC modeling, EKF sensor fusion, and collision-based mode switching provides a lightweight yet powerful toolset for planning and simulating continuum robot locomotion in constrained environments. Future work will focus on physical prototyping, incorporation of dynamic and frictional effects, and real-time curvature estimation from onboard sensing.

VII. Limitations and Future Work

This study did not incorporate real IMU measurements due to the lack of sufficiently rich comparative datasets, which limited our ability to demonstrate the advantages of GTSAM-based optimization. In future work, we plan to:

- **Collect and preprocess real IMU data.** Build a physical prototype instrumented with high-precision inertial measurement units. Perform extended trials under varying bending, vibration, and temperature conditions, and develop robust filtering and denoising pipelines to supply high-quality sensor streams for algorithm evaluation.
- **Quantitatively evaluate GTSAM optimization.** Integrate real IMU data and PCC model predictions into a factor-graph framework using GTSAM. Compare its performance against EKF and batch least-squares in terms of estimation accuracy, convergence rate, and computational cost.
- **Implement online parameter calibration.** Leverage discrepancies between IMU readings and an external ground-truth system (e.g. optical tracker or laser scanner) to adaptively tune key PCC parameters—such as section stiffness and curvature coefficients—thereby improving model fidelity over time.
- **Incorporate friction and dynamics.** Extend the current kinematic-only model by adding pipe-wall friction, material viscoelasticity, and actuator dynamics. Embed these effects into the estimation framework (EKF or factor graph) to predict and control more realistic contact behaviors.
- **Develop closed-loop control and conduct experiments.** Design and implement PID, MPC, or learning-based controllers that leverage the optimized state estimates. Validate climbing performance, energy consumption, and robustness in a physical pipe environment, and compare experimental results against simulation predictions.

By addressing these points, this study aims to fully showcase the benefits of GTSAM optimization, enhance the realism

of the pipe-climbing simulations, and ultimately enable reliable, high-performance continuum-robot operation in confined environments.

ACKNOWLEDGMENT

Shuhan would like to thank Professor Xiaonan Huang for providing me with the invaluable opportunity to independently explore research in ROB590 and welcoming me into a stimulating laboratory environment. The weekly group meetings have been an exceptional platform for learning and intellectual growth. Special thanks to PhD candidate Wenzhe Tong for his patient guidance and insightful feedback throughout this journey.

REFERENCES

[1] Sven Lilge, Timothy Barfoot, and Jessica Burgner-Kahrs. State estimation for continuum multirobot systems on SE(3). *IEEE Transactions on Robotics*, 41:905–920, 2025.

[2] Francesco Stella, Cosimo Della Santina, and Josie Hughes. Soft robot shape estimation with IMUs leveraging PCC kinematics for drift filtering. *IEEE Robotics and Automation Letters*, 9(2):1945–1952, 2024.

[3] Weicheng Fan, Jiaqi Wang, Zhuang Zhang, Genliang Chen, and Hao Wang. Vacuum-driven parallel continuum robots with self-sensing origami linkages. *IEEE/ASME Transactions on Mechatronics*, 29(5):3370–3381, 2024.